JM PAPERS

# Prandtl number effects on passive scalars in turbulent pipe flow

**Sergio Pirozzoli**†

Dipartimento di Ingegneria Meccanica e Aerospaziale, Sapienza Università di Roma, Via Eudossiana 18, 00184 Roma, Italy

We study the statistics of passive scalars (either temperature or concentration of a diffusing substance) at friction Reynolds number $Re_\tau = 1140$, for turbulent flow within a smooth straight pipe of circular cross-section, in the range of Prandtl numbers from $Pr = 0.00625$, to $Pr = 16$, using direct numerical simulations (DNS) of the Navier–Stokes equations. Whereas the organization of passive scalars is similar to the axial velocity field at $Pr = O(1)$, similarity is impaired at low Prandtl number, at which the buffer-layer dynamics is filtered out, and at high Prandtl number, at which the passive scalar fluctuations become confined to the near-wall layer. The mean scalar profiles at $Pr \gtrsim 0.0125$ are found to exhibit logarithmic overlap layers, and universal parabolic distributions in the core part of the flow. Near-universality of the eddy diffusivity is exploited to derive accurate predictive formulas for the mean scalar profiles, and for the corresponding logarithmic offset function. Asymptotic scaling formulas are derived for the thickness of the conductive (diffusive) layer, for the peak scalar variance, and its production rate. The DNS data are leveraged to synthesize a modified form of the classical predictive formula of Kader & Yaglom (*Intl J. Heat Mass Transfer*, vol. 15, 1972, pp. 2329–2351), which is capable of accounting accurately for the dependence on both Reynolds and Prandtl numbers, for $Pr \gtrsim 0.25$.

**Key words:** pipe flow boundary layer, turbulence simulation

## 1. Introduction

The study of passive scalars evolving within wall-bounded turbulent flows has great practical importance, being relevant for the behaviour of diluted contaminants, and/or as a model for the temperature field under the assumption of low Mach number and small

† Email address for correspondence: sergio.pirozzoli@uniroma1.it

temperature differences (Monin & Yaglom 1971; Cebeci & Bradshaw 1984). It is well known that measurements of concentration of passive tracers and of small temperature differences are quite difficult, and in fact available information about even basic passive scalar statistics is rather limited (Gowen & Smith 1967; Kader 1981; Subramanian & Antonia 1981; Nagano & Tagawa 1988), mostly including basic mean properties and overall mass or heat transfer coefficients. The physical understanding of passive scalars in turbulent flow pertains mainly to the case $Pr \approx 1$ (where the molecular Prandtl number is defined here as the ratio of the kinematic viscosity to the thermal diffusivity, $Pr = \nu/\alpha$), for which strong analogies exist between passive scalars and the longitudinal velocity component, as verified in a number of studies (Kim, Moin & Moser 1987; Abe & Antonia 2009; Antonia, Abe & Kawamura 2009). However, many fluids, including water, engine oils, glycerol and polymer melts, have values of $Pr$ that can be significantly higher than unity, whereas in liquid metals and molten salts, the Prandtl number can be much less than unity. In the case of diffusions of contaminants, the Prandtl number is replaced by the Schmidt number (namely, the ratio of kinematic viscosity to mass diffusivity), whose typical values in applications are always much higher than unity (Levich 1962). Under such circumstances, similarity between velocity and passive scalar fluctuations is substantially impaired, which makes predictions of even the basic flow statistics quite difficult. In fact, the most complete predictive theory for the behaviour of passive scalars at non-unit Prandtl number relies heavily on classical studies (Levich 1962; Gowen & Smith 1967; Kader & Yaglom 1972), and most predictive formulas for the heat transfer coefficients are based on semi-empirical power-law correlations (Dittus & Boelter 1933; Kays, Crawford & Weigand 1980). Although existing correlations may have sufficient accuracy for engineering design, their theoretical foundations are not firmly established. Furthermore, assumptions typically made in turbulence models, such as constant turbulent Prandtl number, are known to be crude approximations in the absence of reliable reference data.

Given this scenario, direct numerical simulations (DNS) are the natural candidates to establish a credible database for the physical analysis of passive scalars in wall turbulence, and for the development and validation of phenomenological prediction formulas and turbulence models. Most DNS studies of passive scalars in wall turbulence so far have been carried out for the prototype case of planar channel flow, starting with the work of Kim & Moin (1989), at $Re_\tau = 180$ (here $Re_\tau = u_\tau h/\nu$ is the friction Reynolds number, with $u_\tau = (\tau_w/\rho)^{1/2}$ the friction velocity, $h$ the channel half-height, $\nu$ the fluid kinematic viscosity, $\rho$ the fluid density, and $\tau_w$ the wall shear stress), in which the forcing of the scalar field was achieved using a spatially and temporally uniform source term. Additional DNS at increasingly high Reynolds number were carried out by Kawamura, Abe & Matsuo (1999) and Abe, Kawamura & Matsuo (2004), based on enforcement of strictly constant heat flux in time (this approach is hereafter referred to as CHF), which first allowed us to appreciate scale separation effects, and to educe a reasonable value of the scalar von Kármán constant $k_\theta \approx 0.43$, as well as effects of Prandtl number variation. Those studies showed close similarity between the streamwise velocity and passive scalar field in the near-wall region, as after the classical Reynolds analogy. Specifically, the scalar field was found to be organized into streaks whose size scales in wall units, with a correlation coefficient between streamwise velocity fluctuations and scalar fluctuations close to unity. Computationally high Reynolds numbers ($Re_\tau \approx 4000$, with $Pr \leq 1$) were reached in the study of Pirozzoli, Bernardini & Orlandi (2016), using spatially uniform forcing in such a way as to maintain the bulk temperature constant in time (this approach is hereafter referred to as CMT). Recent large-scale channel flow DNS with passive scalars

using the CHF forcing at $Pr = 0.71$ (as representative of air) have been carried out by Alcántara-Ávila, Hoyas & Pérez-Quiles (2021). Prandtl number effects in plane channel flow were further addressed by Schwertfirm & Manhart (2007), Alcántara-Ávila, Hoyas & Pérez-Quiles (2018), Abe & Antonia (2019), and Alcántara-Ávila & Hoyas (2021), to which we will refer for comparison.

Flow in a circular pipe is clearly more practically relevant than plane channel flow in view of applications as heat exchangers, and it has been the subject of a number of experimental studies, aimed mainly at predicting the heat transfer coefficient as a function of the bulk flow Reynolds number (Kays *et al.* 1980). High-fidelity numerical simulations including passive scalars in pipe flow so far have been quite scarce, and limited mainly to $Re_\tau \leq 1000$ (Piller 2005; Redjem-Saad, Ould-Rouiss & Lauriat 2007; Saha *et al.* 2011; Antoranz *et al.* 2015; Straub *et al.* 2019). Higher Reynolds numbers (up to $Re_\tau = 6000$) have been considered by Pirozzoli *et al.* (2022), but at unit Prandtl numbers. Those DNS confirmed a general similarity between the axial velocity field and the passive scalar field; however, the latter was found to have additional energy at small wavenumbers, resulting in higher mixedness. Logarithmic growth of the inner-scaled bulk and mean centreline scalar values with the friction Reynolds number was found, implying an estimated scalar von Kármán constant $k_\theta \approx 0.459$, similar to what was found in plane channel flow (Pirozzoli *et al.* 2016; Alcántara-Ávila *et al.* 2021). The DNS data were also used to synthesize a modified form of the classical predictive formula of Kader & Yaglom (1972). It appears that DNS data of pipe flow at both high and low Prandtl number have not been explored intensely, despite their importance.

In this paper, we thus present novel DNS data of turbulent flow in a smooth circular pipe at moderate Reynolds number $Re_\tau = 1140$, which is, however, high enough that a state of fully developed turbulence is established, with a near-logarithmic region of the mean velocity profile. A wide range of Prandtl numbers is considered, from $Pr = 0.00625$ to $Pr = 16$, such that some asymptotic properties for vanishing and very high Prandtl number can be inferred. This study complements our previous study about Reynolds number effects (up to $Re_\tau \approx 6000$) for passive scalars at $Pr = 1$ (Pirozzoli *et al.* 2022), allowing predictive extrapolations to the full range of Reynolds and Prandtl numbers. Although, as pointed out previously, the study of passive scalars is relevant in several contexts, one of the primary fields of application is heat transfer, therefore from now on, we will refer to the passive scalar field as the temperature field (denoted as $T$), and scalar fluxes will be interpreted as heat fluxes.

## 2. The numerical dataset

Numerical simulations of fully developed turbulent flow in a circular pipe are carried out assuming periodic boundary conditions in the axial ($z$) and azimuthal ($\phi$) directions, as shown in figure 1. The velocity field is controlled by two parameters, namely the bulk Reynolds number $Re_b = 2Ru_b/\nu$ (with $u_b$ the bulk velocity, i.e. averaged over the cross-section), and the relative pipe length $L_z/R$. The incompressible Navier–Stokes equations are supplemented with the transport equation for a passive scalar field (hence buoyancy effects are disregarded), with different values of the thermal diffusivity (hence various $Pr$), and with isothermal boundary conditions at the pipe wall ($r = R$). The passive scalar equation is forced through a time-varying, spatially uniform source term (CMT approach), in the interests of achieving complete similarity with the streamwise momentum equation, with obvious exclusion of pressure. Although the total heat flux resulting from the CMT approach is not strictly constant in time, it oscillates around
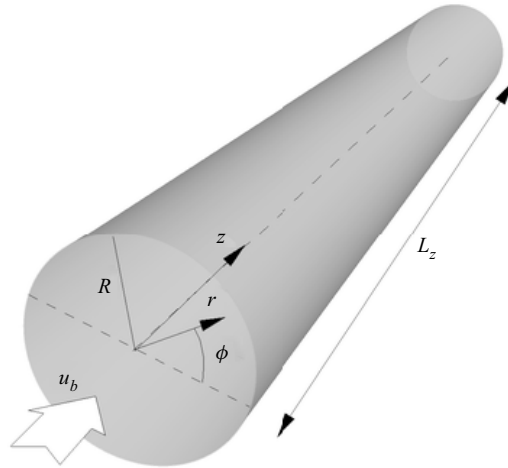
Figure 1. Definition of coordinate system for DNS of pipe flow, where $z$, $r$, $\phi$ are the axial, radial and azimuthal directions, respectively, $R$ is the pipe radius, $L_z$ is the pipe length, and $u_b$ is the bulk velocity.

its mean value under statistically steady conditions. Differences of the results obtained with the CMT and CHF approaches have been pinpointed by Abe & Antonia (2017) and Alcántara-Ávila *et al.* (2021), which, although generally small, deserve some attention.

The computer code used for the DNS is the evolution of the solver developed originally by Verzicco & Orlandi (1996), and used for DNS of pipe flow by Orlandi & Fatica (1997). The solver relies on second-order finite-difference discretization of the incompressible Navier–Stokes equations in cylindrical coordinates based on the classical marker-and-cell method (Harlow & Welch 1965), whereby pressure and passive scalars are located at the cell centres, whereas the velocity components are located at the cell faces, thus removing odd–even decoupling phenomena, and guaranteeing discrete conservation of the total kinetic energy and passive scalar variance in the inviscid limit. The Poisson equation resulting from enforcement of the divergence-free condition is solved efficiently by double trigonometric expansion in the periodic axial and azimuthal directions, and inversion of tridiagonal matrices in the radial direction (Kim & Moin 1985). A crucial computational issue is the proper treatment of the polar singularity at the pipe axis, which we handle as suggested by Verzicco & Orlandi (1996), by replacing the radial velocity $u_r$ in the governing equations with $q_r = r u_r$ (where $r$ is the radial space coordinate), which by construction vanishes at the axis. The governing equations are advanced in time by means of a hybrid third-order low-storage Runge–Kutta algorithm, whereby the diffusive terms are handled implicitly, and convective terms in the axial and radial direction explicitly. An important issue in this respect is the convective time step limitation in the azimuthal direction, due to intrinsic shrinking of the cell size towards the pipe axis. To alleviate this limitation, we use implicit treatment of the convective terms in the azimuthal direction (Akselvoll & Moin 1996; Wu & Moin 2008), which enables marching in time with a time step similar to that in planar domain flow in practical computations. In order to minimize numerical errors associated with implicit time stepping, explicit and implicit discretizations of the azimuthal convective terms are blended linearly with the radial coordinate, in such a way that near the pipe wall, the treatment is fully explicit, and near the pipe axis, it is fully implicit. The code was adapted to run on clusters of graphic accelerators (GPUs), using a combination of CUDA Fortran and OpenACC directives, and

**965** A7-4

| Prandtl number | Mesh ($N_z \times N_r \times N_\phi$) | $Pe_\tau$ | $Nu$ | ETT | Line style |
|---|---|---|---|---|---|
| 0.00625 | $1792 \times 164 \times 1793$ | 7.11 | 8.02 | 21.3 | |
| 0.0125 | $1792 \times 164 \times 1793$ | 14.2 | 9.41 | 23.1 | |
| 0.025 | $1792 \times 164 \times 1793$ | 28.5 | 12.6 | 36.0 | |
| 0.0625 | $1792 \times 164 \times 1793$ | 71.1 | 21.5 | 23.1 | |
| 0.125 | $1792 \times 164 \times 1793$ | 142.2 | 34.2 | 12.9 | |
| 0.25 | $1792 \times 164 \times 1793$ | 284.4 | 53.8 | 47.7 | |
| 0.5 | $1792 \times 164 \times 1793$ | 568.8 | 81.7 | 20.6 | |
| 1 | $1792 \times 164 \times 1793$ | 1137.6 | 119.9 | 38.1 | |
| 2 | $3584 \times 269 \times 3584$ | 2275.2 | 168.0 | 14.2 | |
| 4 | $3584 \times 269 \times 3584$ | 4550.4 | 233.3 | 10.6 | |
| 16 | $7168 \times 441 \times 7168$ | 18201.6 | 421.2 | 9.51 | |

Table 1. Flow parameters for DNS of pipe flow at various Prandtl numbers. Here, $N_z$, $N_r$, $N_\phi$ denote the numbers of grid points in the axial, radial and azimuthal directions, respectively, $Pe_\tau = Pr\,Re_\tau$ is the friction Péclet number, $Nu$ is the Nusselt number (as defined in (3.25)), and ETT is the time interval considered to collect the flow statistics, in units of the eddy-turnover time, namely $R/u_\tau$. For all simulations, $L_z = 15R$, $Re_b = 44\,000$ and $Re_\tau = 1137.6$.

relying on the CUFFT libraries for efficient execution of fast Fourier transforms (Ruetsch & Fatica 2014).

From now on, inner normalization of the flow properties will be denoted with the '+' superscript, whereby velocities are scaled by $u_\tau$, wall distances ($y = R - r$) by $\nu/u_\tau$, and temperatures with respect to the friction temperature,

$$T_\tau = \frac{\alpha}{u_\tau} \left\langle \frac{dT}{dy} \right\rangle_w. \tag{2.1}$$

In particular, the inner-scaled temperature is defined as $\theta^+ = (T - T_w)/T_\tau$, where $T$ is the local temperature, and $T_w$ is the wall temperature. Capital letters will be used to denote flow properties averaged in the homogeneous spatial directions and in time, brackets to denote the averaging operator, and lower-case letters to denote fluctuations from the mean. Instantaneous values will be denoted with a tilde, e.g. $\tilde{\theta} = \Theta + \theta$. The bulk values of axial velocity and temperature are defined as

$$u_b = 2 \int_0^R r \langle u_z \rangle \, dr \Big/ R^2, \quad T_b = 2 \int_0^R r \langle T \rangle \, dr \Big/ R^2. \tag{2.2a,b}$$

A list of the main simulations that we have carried out is given in table 1. Eleven values of the Prandtl number are considered, from $Pr = 0.00625$ to 16. The pipe length was set to $L_z = 15R$ for all the flow cases, based on a box sensitivity study (Pirozzoli *et al.* 2022). The mesh resolution is designed based on the criteria discussed by Pirozzoli & Orlandi (2021). In particular, the collocation points are distributed in the wall-normal direction so that approximately 30 points are placed within $y^+ \leq 40$, with the first grid point at $y^+ < 0.1$, and the mesh is stretched progressively in the outer wall layer in such a way that the mesh spacing is proportional to the local Kolmogorov length scale, which there varies as $\eta^+ \approx 0.8\,y^{+1/4}$ (Jiménez 2018). Regarding the axial and azimuthal directions, finite-difference simulations of wall-bounded flows yield grid-independent results as long as $\Delta z^+ \approx 10$, $R^+ \Delta\phi \approx 4.5$ (Pirozzoli *et al.* 2016), hence we have selected the number of grid points along the homogeneous flow directions as $N_z = L_z/R \times Re_\tau/9.8$, $N_\phi \sim 2\pi \times Re_\tau/4.1$.

A finer mesh is used for flow cases with $Pr > 1$, so as to satisfy restrictions on the Batchelor scalar dissipative scale, whose ratio to the Kolmogorov scale is approximately $Pr^{-1/2}$ (Batchelor 1959; Tennekes & Lumley 1972).

According to established practice (Hoyas & Jiménez 2006; Ahn *et al.* 2015; Lee & Moser 2015), the time intervals used to collect the flow statistics are reported as a fraction of the eddy-turnover time ($R/u_\tau$). The sampling errors for some key properties discussed in this paper have been estimated using the method of Russo & Luchini (2017), based on extension of the classical batch means approach. We have found that the sampling error is generally quite limited, being larger in the largest DNS, which are, however, carried out over a shorter time interval. In particular, in the $Pr = 16$ flow case, the expected sampling error in Nusselt number, centreline temperature and peak temperature variance is approximately 0.5 %. In order to quantify uncertainties associated with numerical discretization, additional simulations have been carried out by doubling the numbers of grid points in the azimuthal, radial and axial directions. The results show that the uncertainty due to numerical discretization and limited pipe length is approximately 0.2 % for the Nusselt number, 0.4 % for the pipe centreline temperature, and 0.7 % for the peak temperature variance.

## 3. Results

### 3.1. *General organization of the temperature field*

Qualitative information about the organization of the flow field is provided by instantaneous perspective views of the axial velocity and temperature fields, which we show in figures 2–4. As is well known, the flow near the pipe wall is dominated by streaks of alternating high- and low-speed fluid, which are the hallmark of wall-bounded turbulence (figures 2*a*, 3*a*, 4*a*); see Kline *et al.* (1967). The temperature field at unit Prandtl number (figures 2*d*, 3*d*, 4*d*) exhibits a similar organization, which is not surprising on account of close formal similarity of passive scalar and axial momentum equations at $Pr = 1$, and close association of the two quantities was indeed pointed out in many previous studies (e.g. Abe & Antonia 2009; Pirozzoli *et al.* 2016; Alcántara-Ávila *et al.* 2018). Zooming closer (see figure 4), one will nevertheless detect differences between the two fields, in that temperature tends to form sharper fronts, whereas the axial velocity field tends to be more blurred. As noted by Pirozzoli *et al.* (2016), this is due to the fact that the axial velocity is not simply advected passively, but rather it can react to the formation of fronts through feedback pressure. This reflects into shallower spectral ranges than Kolmogorov's $k^{-5/3}$ (Pirozzoli *et al.* 2022). Thermal streaks persist at $Pr > 1$ (figures 2*e*,*f*, 3*e*,*f*, 4*e*,*f*), and seem to retain a similar organization as in the case of unit Prandtl number. However, they tend to vanish at low Prandtl number (figures 2*b*,*c*, 3*b*,*c*, 4*b*,*c*), and are totally suppressed at $Pr = 0.00625$, as a result of scalar diffusivity overwhelming turbulent agitation. The flow in the cross-stream planes (figures 3 and 4) is characterized by sweeps of high-speed fluid from the pipe core and ejections of low-speed fluid from the wall. Ejections and sweep have a clearly multi-scale nature, as some of them are confined to the buffer layer, whereas others manage to protrude up to the pipe centreline. At very low Prandtl number (figures 2*b*, 3*b*, 4*b*), turbulence is barely capable of perturbing the otherwise purely diffusive behaviour of the temperature field. The presence of details on a finer and finer scale is evident at increasing $Pr$, on account of the previously noted reduction of the Batchelor scale. Increase of the Prandtl number also yields progressive equalization of the temperature field over the cross-section. As a result, the large-scale eddies become weaker, and thermal agitation becomes confined mainly to

$$\tilde{u}_z/U_{CL}, \tilde{\theta}/\Theta_{CL}$$

0    0.10  0.15  0.20  0.30  0.40  0.50  0.60  0.70  0.80  0.85  0.90  1.00



Figure 2. (*a*) Instantaneous axial velocity contours, and temperature contours for (*b*) $Pr = 0.00625$, (*c*) $Pr = 0.25$, (*d*) $Pr = 1$, (*e*) $Pr = 4$, and (*f*) $Pr = 16$, each normalized by the mean value at the pipe axis. The near-wall contours are taken at distance $y^+ = 15$.

the wall vicinity, within a layer whose thickness is proportional to the conductive sublayer thickness, which will be discussed extensively later.

The above scenario is substantiated by the spectral maps of $u_z$ and $\theta$, which are depicted in figure 5. The axial velocity spectra (figure 5*a*) clearly bring out a two-scale organization, with a near-wall peak associated with the wall regeneration cycle (Jiménez & Pinelli 1999),

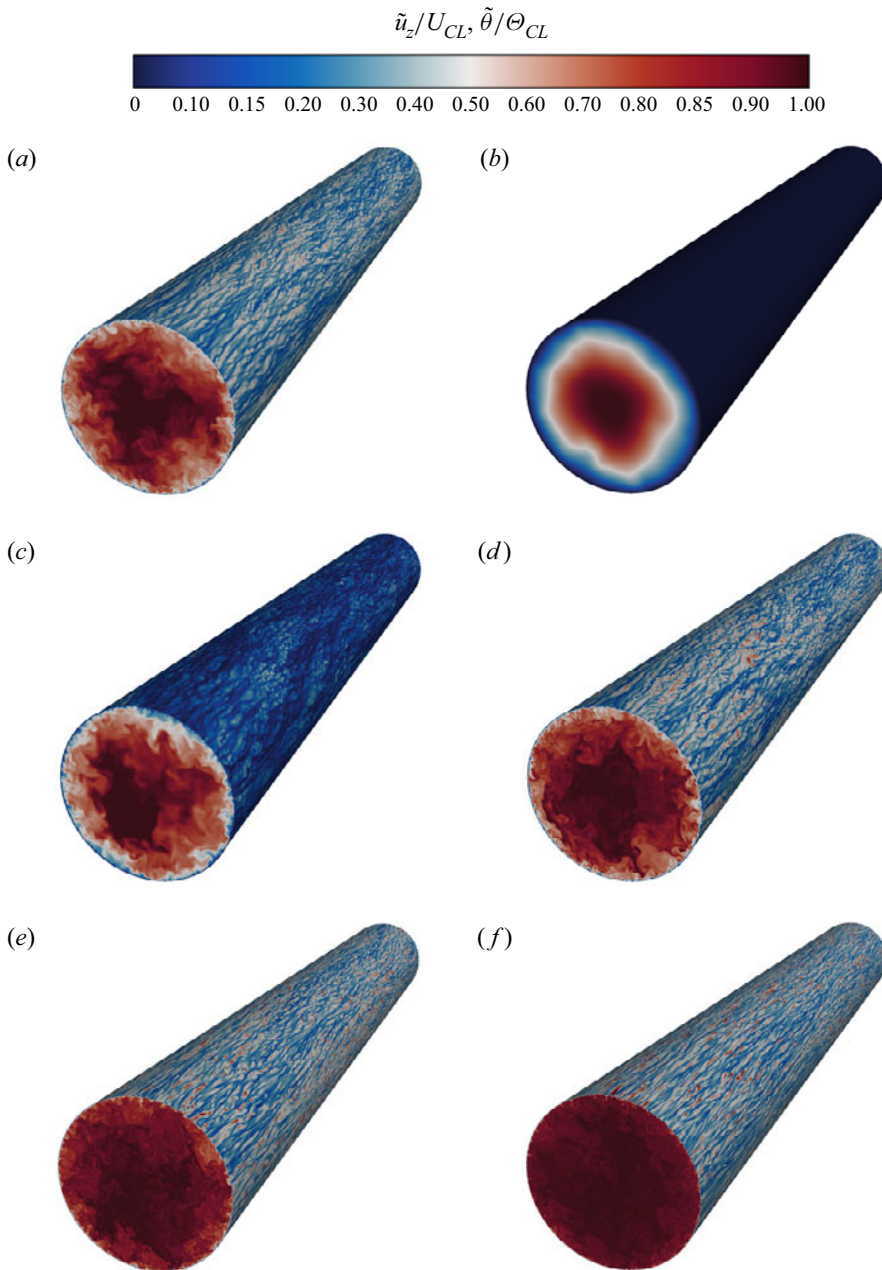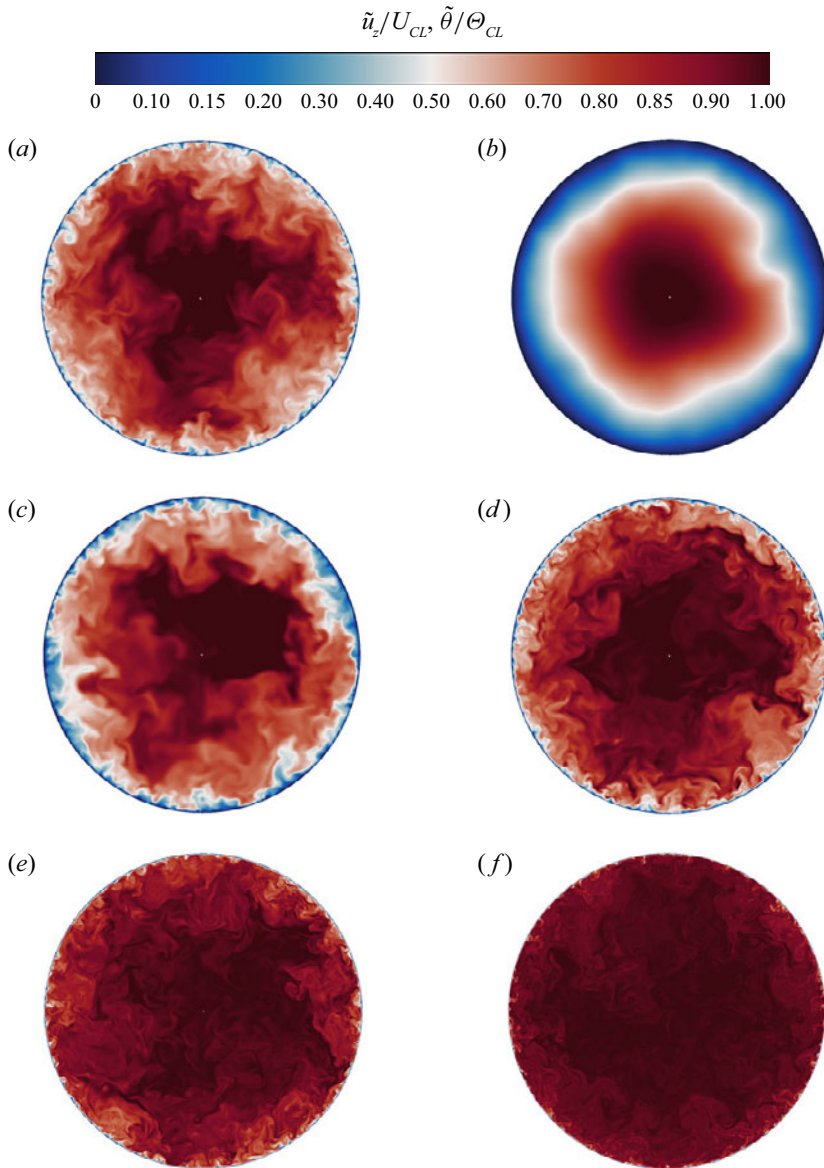$$\tilde{u}_z/U_{CL}, \tilde{\theta}/\Theta_{CL}$$



Figure 3. (*a*) Instantaneous axial velocity contours, and temperature contours for (*b*) $Pr = 0.00625$, (*c*) $Pr = 0.25$, (*d*) $Pr = 1$, (*e*) $Pr = 4$, and (*f*) $Pr = 16$, in a cross-sectional plane, each normalized by the mean value at the pipe axis.

and an outer peak associated with outer-layer large-scale motions (Hutchins & Marusic 2007). The latter peak is found to be centred around $y/R \approx 0.22$, and to correspond to eddies with typical wavelength $\lambda_\phi \approx 1.25R$. Notably, very similar organization is found in the temperature field at unit Prandtl number (figure 5*d*), the main difference being a less distinct energy peak at large wavelengths. Both the axial velocity and the temperature field exhibit a prominent spectral ridge corresponding to modes with typical azimuthal length scale $\lambda_\phi \sim y$, extending over more than one decade, which can be interpreted as the footprint of a hierarchy of wall-attached eddies after Townsend's hypothesis

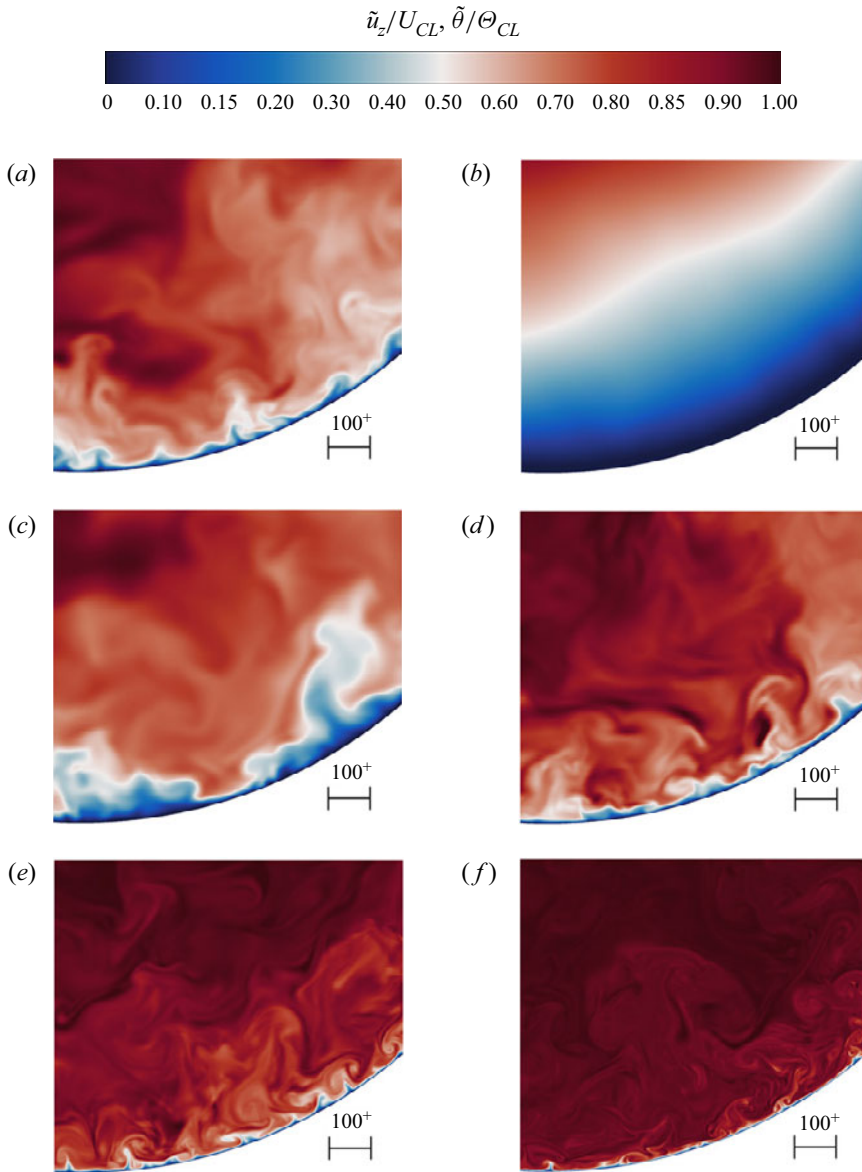$$\tilde{u}_z/U_{CL}, \tilde{\theta}/\Theta_{CL}$$



Figure 4. (*a*) Instantaneous axial velocity contours, and temperature contours for (*b*) $Pr = 0.00625$, (*c*) $Pr = 0.25$, (*d*) $Pr = 1$, (*e*) $Pr = 4$, and (*f*) $Pr = 16$, in a subregion of the pipe cross-section, each normalized by the mean value at the pipe axis. A segment with length of 100 wall units is reported for reference.

(Townsend 1976). The spectral maps are, however, quite different at non-unit Prandtl number. At very low Prandtl number (figure 5*b*), all the small scales of thermal motion are filtered out by the large thermal diffusivity, and hints of organization are found only at the largest scales. The typical azimuthal length scale of these eddies appears to be $\lambda_\phi = \pi R$, hence only two pairs of eddies are found on average. At $Pr = 0.25$ (figure 5*c*), a clear wall-attached spectral ridge is observed, meaning that the temperature field becomes in tune with the wall-attached eddies of Townsend's hierarchy. However, no buffer-layer peak is observed.
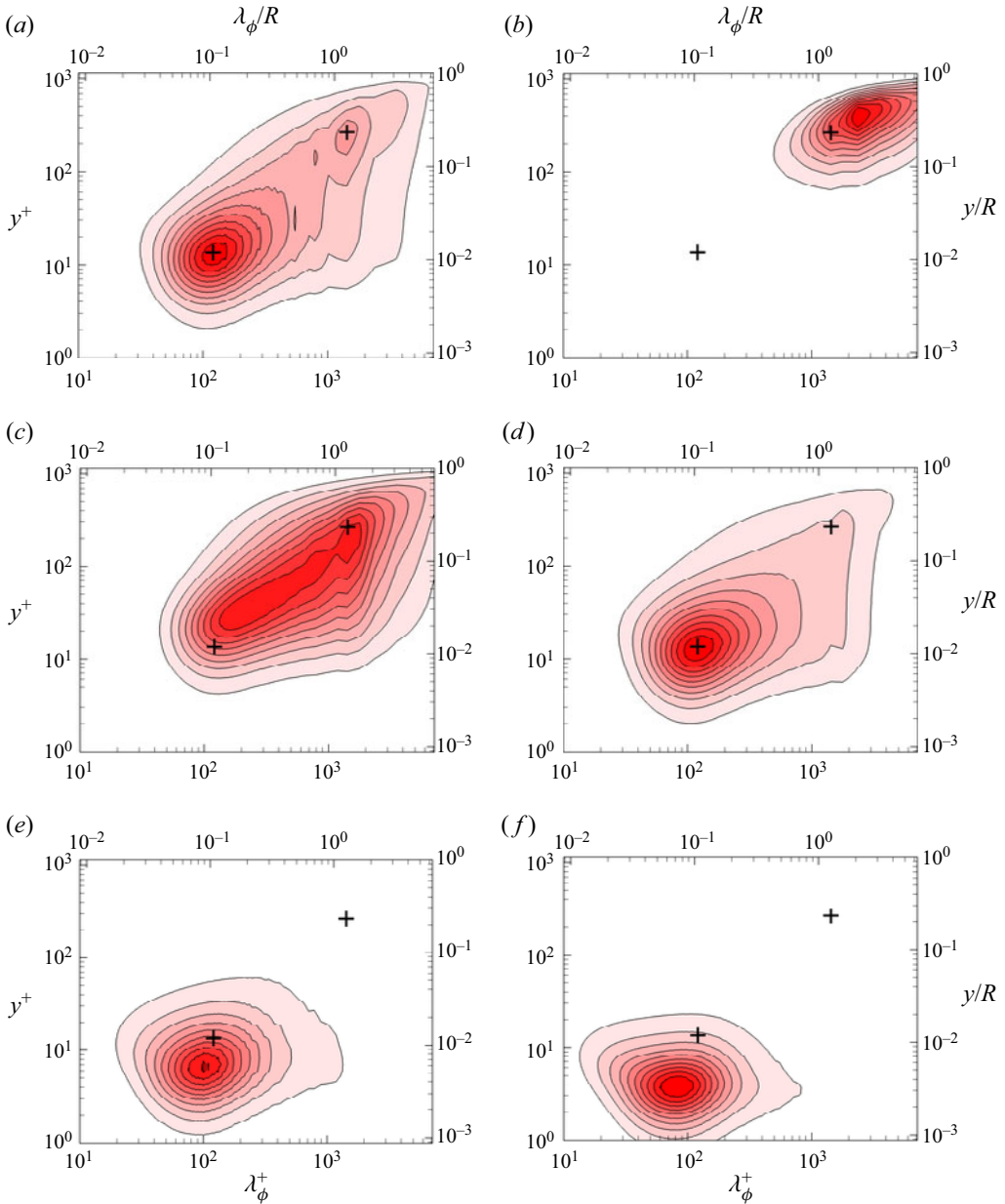
Figure 5. Variation of pre-multiplied spanwise spectral densities with wall distance for (*a*) the axial velocity field, and for the temperature fields corresponding to (*b*) $Pr = 0.00625$, (*c*) $Pr = 0.25$, (*d*) $Pr = 1$, (*e*) $Pr = 4$, and (*f*) $Pr = 16$. For the sake of comparison, each field is normalized by its maximum value, and ten contours are shown. Wall distances (*y*) and azimuthal wavelengths ($\lambda_\phi$) are reported both in inner units (bottom and left-hand axes) and in outer units (top and right-hand axes). The crosses denote the locations of the inner and outer energy sites in the axial velocity spectral maps.

At Prandtl number higher than unity (figures 5*e*,*f*), temperature fluctuations instead become much more energetic within the buffer layer. Specifically, the inner-layer peak moves closer to the wall, and the streak spacing is reduced as compared to the $Pr = 1$ case. Although large-scale outer motions seem to be absent in the selected representation (each

**965** A7-10

spectrum is normalized by the corresponding peak value), reporting the same maps in the same range of values would show that the spectral footprint in the outer region is similar at all Prandtl numbers, with the exception of the lowest values. This is also portrayed well in the distributions of the integrated energy (see figure 12).

It is interesting that the spectral densities along the axial direction, shown in figure 6, still show a shift of the main energetic site along the vertical direction with the Prandtl number; however, the typical axial length scale is weakly affected. This relative insensitivity is also clear from looking at the streaks meandering in figure 2. The different behaviours of the azimuthal and axial spectra can be explained by interpreting the temperature field as resulting from the application of a filter to the velocity field. Variation of the Prandtl number then has the effect of changing the filter cutoff. Since the azimuthal scale of the streaks is comparatively smaller, the effect of filtering is more evident, whereas the longitudinal scale associated with streaks meandering is much larger, hence the effect of filtering is less visible, unless very low Prandtl numbers are considered.

### 3.2. *Temperature statistics*

The mean temperature profiles in turbulent pipes have received extensive attention from theoretical and experimental studies, and the general consensus (Kader 1981) is that a logarithmic law is a good approximation in the overlap layer, for most practical purposes. The recent study of Pirozzoli *et al.* (2021) has shown that at unit Prandtl number, the logarithmic law fits well with the mean temperature profile in the overlap layer, with Kármán constant $k_\theta = 0.459$, which is distinctly larger than for the axial velocity field, namely $k = 0.387$. Figure 7(*a*) confirms, as is well known, that universality with respect to *Pr* variations is not achieved in inner scaling, since the asymptotic behaviour in the conductive sublayer is $\Theta^+ \approx Pr\, y^+$ (see e.g. Kawamura *et al.* 1998). The figure also shows that visually logarithmic distributions are obtained in a wide range of Prandtl numbers, namely

$$\Theta^+ = \frac{1}{k_\theta} \log y^+ + \beta(Pr), \tag{3.1}$$

with clear change of the additive constant $\beta$, as pointed out by Kader & Yaglom (1972). The effect of Prandtl number variation on the outer layer is analysed in figure 7(*b*), where we show the mean temperature profiles in defect form, namely in terms of difference from the centreline value. Assuming $y^+ = 100$ to be the root of the logarithmic layer for the mean velocity profile (Pirozzoli *et al.* 2021), this amounts for the flow cases herein considered to $y/R \approx 0.11$. The figure shows that scatter across the defect temperature profiles at various *Pr* is quite small farther from the wall, which suggests that outer-layer similarity applies with good precision in general. Departures from outer-layer universality are observed starting at $Pr \lesssim 0.025$, below which the similarity region becomes narrower and progressively confined to the region around the pipe axis. As suggested by Pirozzoli (2014) and Orlandi, Bernardini & Pirozzoli (2015), the core velocity and temperature profiles can be approximated closely with simple universal quadratic distributions, which one can derive under the assumption of constant eddy diffusivity of momentum and temperature. In particular, we find that the expression

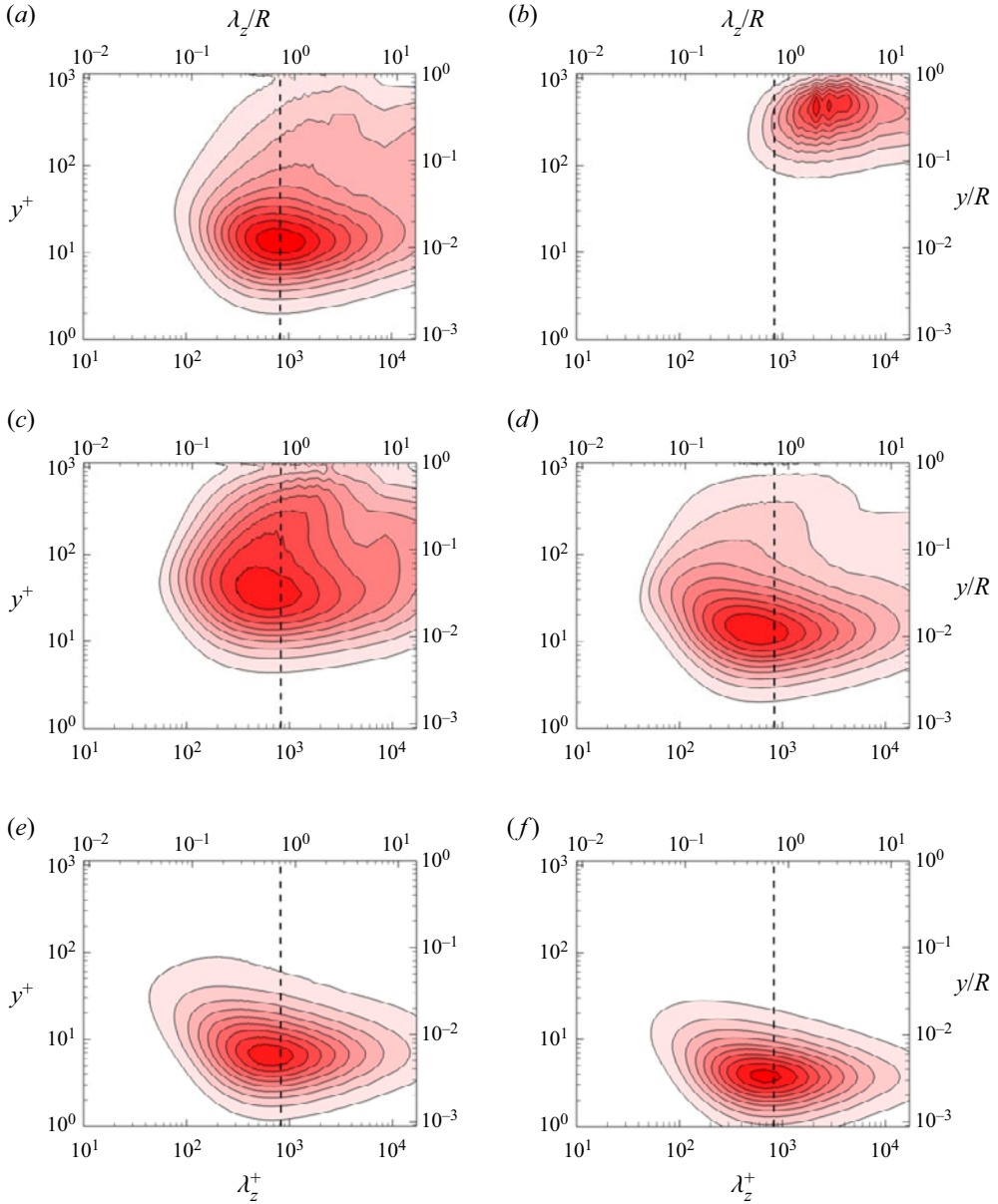$$\Theta^+_{CL} - \Theta^+ = C_\theta \left(1 - y/R\right)^2, \tag{3.2}$$

Figure 6. Variation of pre-multiplied axial spectral densities with wall distance for (*a*) the axial velocity field, and for the temperature fields corresponding to (*b*) $Pr = 0.00625$, (*c*) $Pr = 0.25$, (*d*) $Pr = 1$, (*e*) $Pr = 4$, and (*f*) $Pr = 16$. For the sake of comparison, each field is normalized by its maximum value, and ten contours are shown. Wall distances (*y*) and axial wavelengths ($\lambda_z$) are reported both in inner units (bottom and left-hand axes) and in outer units (top and right-hand axes). The vertical dashed lines mark the peak wavelengths in the spectra of the axial velocity ($\lambda_z^+ \approx 820$).

with $C_\theta = 6.62$, fits the mean temperature distributions in the pipe core ($y \geq 0.2R$) quite well. Closer to the wall, the defect logarithmic wall law sets in at $y/R \lesssim 0.2$,

$$\Theta_{CL}^+ - \Theta^+ = -\frac{1}{k_\theta} \log(y/R) + B_\theta, \tag{3.3}$$
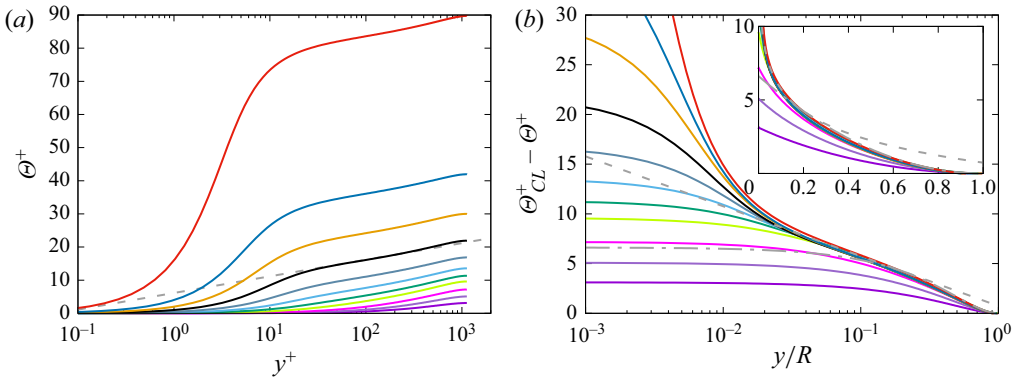
Figure 7. (*a*) Inner-scaled mean temperature profiles, and (*b*) corresponding defect profiles. The dashed grey line in (*a*) refers to the assumed logarithmic wall law for $Pr = 1$, namely $\Theta^+ = \log y^+/0.459 + 6.14$. In (*b*), the dash-dotted grey line marks a parabolic fit of the DNS data, $\Theta_{CL}^+ - \Theta^+ = 6.62(1 - y/R)^2$, and the dashed grey line marks the outer-layer logarithmic fit $\Theta_{CL}^+ - \Theta^+ = 0.732 - 1/0.459 \log(y/R)$. See table 1 for colour codes.

where data fitting in the range $y^+ \geq 50$, $y/R \leq 0.2$, yields $B_\theta = 0.732$.

Modelling the turbulent heat fluxes requires closures with respect to the mean temperature gradient (see e.g. Cebeci & Bradshaw 1984), through the introduction of a thermal eddy diffusivity, defined as

$$\alpha_t = \frac{\langle u_r \theta \rangle}{\mathrm{d}\Theta/\mathrm{d}y}. \tag{3.4}$$

Figure 8 shows that the inferred turbulent thermal diffusivities have a rather simple distribution. Figure 8(*a*) shows near collapse of all cases to a common distribution, noting that a log-log scale is used to better bring out the near-wall behaviour. Cases with $Pr \lesssim 0.125$ fall outside the universal trend, as they show a similarly shaped distribution of $\alpha_t$, but lower absolute values. In agreement with asymptotic arguments (Kader & Yaglom 1972), the limiting near-wall behaviour is $\alpha_t \sim y^3$. Farther from the wall, there is evidence for a narrow region with linear growth of $\alpha_t$, which is the hallmark of logarithmic behaviour of the temperature profiles, and which is much clearer at $Re_\tau = 6000$; see the black dotted line in the figure. In most modelling approaches (Kays *et al.* 1980; Cebeci & Bradshaw 1984), the eddy diffusivity is expressed in terms of the eddy viscosity ($\nu_t = \langle u_r u_z \rangle/(\mathrm{d}U_z/\mathrm{d}y)$), by introducing the turbulent Prandtl number, defined as $Pr_t = \nu_t/\alpha_t$. Although this is generally assumed to be of the order of unity, a rather complex behaviour is observed in practice, as the inset of figure 8(*a*) shows, and as noted by previous authors (Alcántara-Ávila *et al.* 2018; Abe & Antonia 2019; Alcántara-Ávila & Hoyas 2021).

The distributions of $\alpha_t$ in the near-wall and logarithmic regions can be modelled using a suitable functional expression, which we borrow from the Johnson–King turbulence model (Johnson & King 1985), namely

$$\alpha_t^+ = k_\theta y^+ D(y^+), \quad D(y^+) = \left(1 - \mathrm{e}^{-y^+/A_\theta}\right)^2, \tag{3.5a,b}$$

in which the damping function has the asymptotic behaviours

$$D(y^+) \overset{y^+ \to 0}{\approx} y^{+2}/A_\theta^2, \quad D(y^+) \overset{y^+ \to \infty}{\approx} 1. \tag{3.6a,b}$$
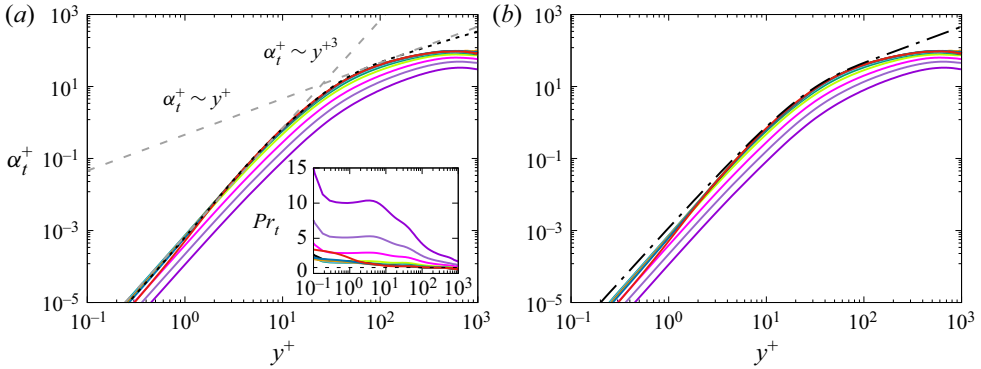
**965** A7-13

Figure 8. Distributions of inferred eddy thermal diffusivity ($\alpha_t$) as a function of wall distance. In (*a*), the black dotted line denotes $\alpha_t$ for the case $Re_\tau = 6000$ at $Pr = 1$ (Pirozzoli *et al.* 2022), and the grey dashed lines denote the asymptotic trends $\alpha_t^+ \sim y^3$ towards the wall, and $\alpha_t^+ = k_\theta y^+$ in the log layer. The inset shows the distribution of the turbulent Prandtl number, the dashed grey line denoting the expected value in the logarithmic layer, namely $Pr_t = k/k_\theta \approx 0.84$. In (*b*), the dash-dotted line denotes the fit given in (3.5*a,b*). Colour codes are as in table 1.

Figure 8(*b*) shows that (3.5*a,b*) with $A_\theta = 19.2$ yields a nearly perfect fit of the DNS data, with slight deviations at $y^+ \lesssim 10$, where in any case the eddy diffusivity is much less than the molecular one.

Starting from the mean thermal balance equation,

$$\frac{1}{Pr} \frac{\mathrm{d}\Theta^+}{\mathrm{d}y^+} + \langle u_r \theta \rangle^+ = 1 - y^+/Re_\tau, \tag{3.7}$$

and under the inner-layer assumption ($y^+/Re_\tau \ll 1$), one can then infer the distribution of the mean temperature in the inner layer from knowledge of the eddy thermal diffusivity, by integrating

$$\frac{\mathrm{d}\Theta^+}{\mathrm{d}y^+} = \frac{Pr}{1 + k_\theta \, Pr \, y^+ \, D(y^+)}. \tag{3.8}$$

As figure 9 shows clearly, the quality of the resulting reconstructed temperature profiles is generally very good, with the obvious exception of the outermost region of the flow. Deviations from the predicted trends are observed at the lowest Prandtl numbers ($Pr \lesssim 0.125$), which, as previously observed, escape from the universal trend of $\alpha_t$.

An important property to define the behaviour of passive scalars in wall-bounded flows is the thickness of the conductive sublayer. The latter has been given several definitions (see e.g. Levich 1962; Schwertfirm & Manhart 2007; Alcántara-Ávila & Hoyas 2021); however, we believe that the most obvious is the wall distance at which the turbulent heat flux equals the conductive one, which, based on (3.7), occurs when

$$\alpha_t^+(\delta_t^+) = \frac{1}{Pr}. \tag{3.9}$$

Assuming the validity of the closure (3.5*a,b*), for $Pr \ll 1$ the latter condition yields

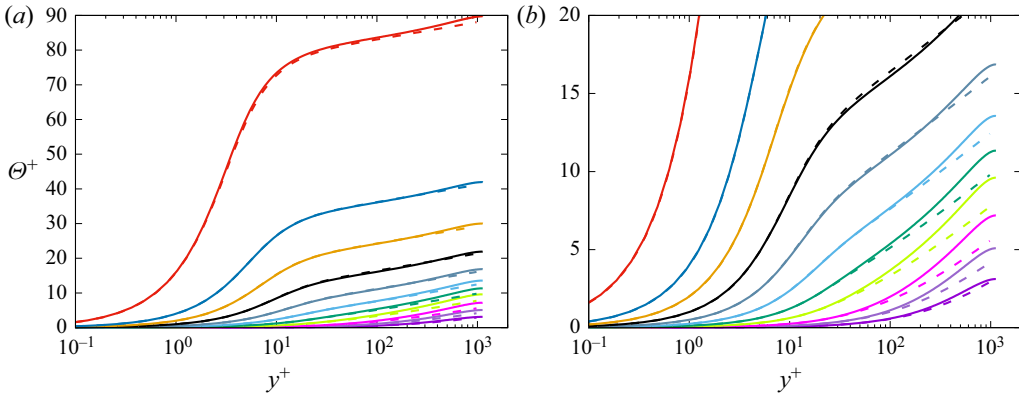$$\delta_t^+ \approx \frac{1}{k_\theta \, Pr}, \tag{3.10}$$

Figure 9. Comparison of mean temperature profiles obtained from DNS (solid lines) and from (3.8), with the eddy diffusivity model (3.5a,b) (dashed lines). Panel (b) shows a magnified view to emphasize the behaviour of the low-*Pr* cases.
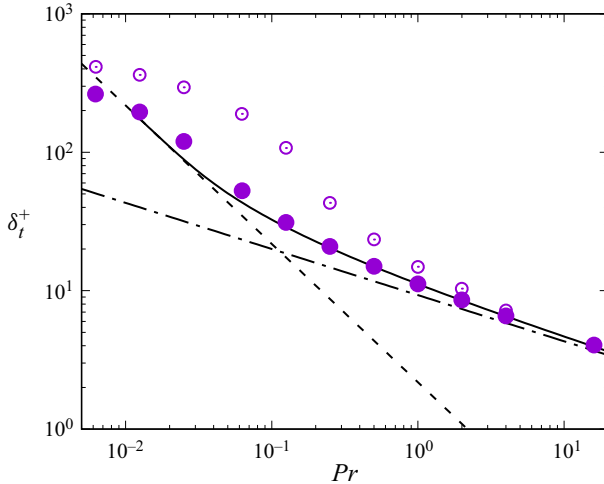


Figure 10. Thickness of the conductive sublayer, estimated from equality of turbulent and conductive heat flux (solid symbols), and position of temperature variance peak (open symbols), compared with predictions of the eddy diffusivity model (3.9) (solid line), and with the low-Prandtl-number approximation (3.10) (dashed line) and the high-Prandtl-number approximation (3.11) (dash-dotted line).

whereas for $Pr \gg 1$ one obtains

$$\delta_t^+ \approx \left( \frac{A_\theta^2}{k_\theta \, Pr} \right)^{1/3}. \tag{3.11}$$

Figure 10 compares the above asymptotic estimates, as well as the estimate obtained by solving (3.9) using the full approximation of the eddy diffusivity (3.5a,b), with the actual DNS data. Again, very good agreement is recovered at $Pr \gtrsim 0.125$, for which $\alpha_t$ is modelled accurately from (3.5a,b), whereas deviations appear at lower *Re*. Whereas the high-Prandtl-number scaling $\delta_t^+ \sim Pr^{-1/3}$ implied by (3.11) was questioned in several previous studies (Na, Papavassiliou & Hanratty 1999; Schwertfirm & Manhart 2007), we find that it applies to the DNS data quite well. Possible reasons may reside in the fact

that previous studies were conducted at much lower Reynolds number, at which scale separation between inner and outer layer was not substantial. Much less clear is the limit of low Prandtl numbers, for which (3.10) yields a qualitatively correct increasing trend, although with large quantitative deviations. With this caveat, the estimate (3.10) can also be exploited to derive minimal conditions for the establishment of a logarithmic layer in the mean temperature distribution. In fact, setting the edge of the log layer to $y/R \approx 0.2$, the conductive sublayer is contained in it only as long as $0.2 k_\theta \, Pr \, Re_\tau \geq 1$, which implies $Pe_\tau \geq 10.9$, where $Pe_\tau = Pr \, Re_\tau$ is the friction Péclet number. This condition is not satisfied in the present dataset from the $Pr = 0.00625$ flow case, and it is barely satisfied in the $Pr = 0.0125$ case (see table 1).

From (3.8), one can also infer approximate values for the log-law additive constant in (3.1), defined as

$$\beta(Pr) = \lim_{y^+ \to \infty} \left( \Theta^+(y^+) - \frac{1}{k_\theta} \log y^+ \right), \tag{3.12}$$

which are crucial in the estimation of the heat transfer coefficient (see below). Explicit approximations for the log-law shift can be obtained in the limits of very low and very high Prandtl numbers. For $Pr \ll 1$, (3.8) readily yields

$$\Theta^+ \approx \frac{1}{k_\theta} \log(k_\theta \, Pr \, y^+), \tag{3.13}$$

which implies

$$\beta(Pr) = \frac{1}{k_\theta} \log Pr + \frac{\log k_\theta}{k_\theta}. \tag{3.14}$$

On the other hand, for $Pr \gg 1$, integrating (3.8) yields

$$\begin{aligned}
\Theta^+ &\approx \int_0^{y^+} \left( \frac{Pr}{1 + k_\theta \, Pr \, \eta} + \frac{Pr}{1 + k_\theta \eta^3 / Pr} \right) \mathrm{d}\eta \\
&= \frac{\sqrt{3}}{6} \pi \left( \frac{A_\theta^2 \, Pr^2}{k_\theta} \right)^{1/3} - \frac{1}{k_\theta} \log(A_\theta k_\theta \, Pr) + \frac{1}{k_\theta} \log(k_\theta \, Pr \, y^+),
\end{aligned} \tag{3.15}$$

which implies

$$\beta(Pr) = \frac{\sqrt{3} \, \pi A_\theta^{2/3}}{6 k_\theta^{1/3}} Pr^{2/3} + \frac{1}{k_\theta} \log Pr - \frac{1}{k_\theta} \log A_\theta. \tag{3.16}$$

We note that a similar functional approximation for $\beta(Pr)$ was arrived at by Kader & Yaglom (1972), although based partly on empiricism and data fitting.

Changes of the additive logarithmic constant with $Pr$ are examined in figure 11. In figure 11(*a*), we illustrate the procedure that we have followed in order to obtain estimates of the $\beta(Pr)$ function, based on fitting the mean temperature distributions with logarithmic functions with prefactor $k_\theta = 0.459$. It is quite interesting that logarithmic distributions are recovered for all cases, apart from the $Pr = 0.00625$ case, consistently with the previously obtained lower bounds for the existence of a logarithmic layer of the mean temperature. Figure 11(*b*) then compares the log-law offset constant thus inferred from the DNS temperature profiles, with the estimate obtained from (3.12), and $\Theta$ resulting from numerical integration of (3.8), as well as with the low- and high-$Pr$ asymptotics.
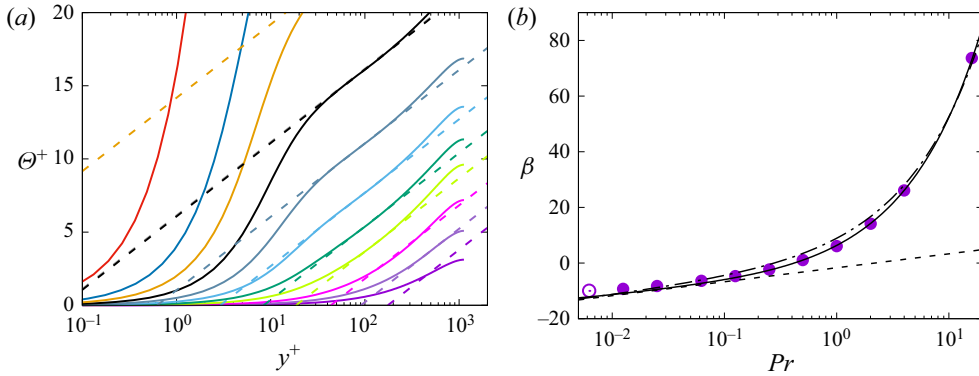
Figure 11. (*a*) Determination of the log-law offset function, and (*b*) its distribution as a function of *Pr*. In (*a*), the dashed lines denote logarithmic best fits of the DNS data, of the form $\Theta^+ = (1/k_\theta) \log y^+ + \beta$. In (*b*), the solid line refers to the estimate obtained from (3.12), with $\Theta$ obtained from numerical integration of (3.8), the dashed line refers to the low-*Pr* asymptote (3.14), and the dash-dotted line refers to the high-*Pr* asymptote (3.16). The case $Pr = 0.00625$ is marked with an open symbol.
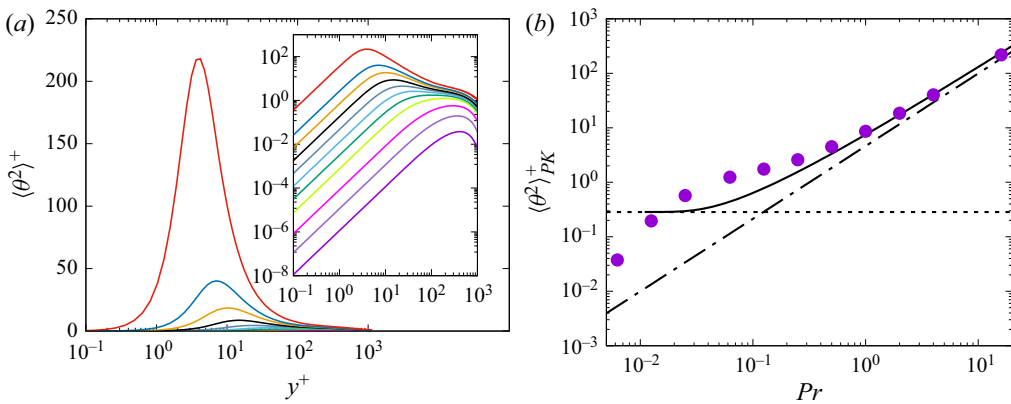


Figure 12. Distributions of (*a*) temperature variances, and (*b*) corresponding peak value as a function of *Pr*. In (*b*), the solid line denotes the predictions of (3.18), the dash-dotted line denotes the high-*Pr* asymptote (3.19), and the dashed line denotes the low-*Pr* asymptote (3.20). Refer to table 1 for colour codes.

The prediction of $\beta$ obtained from numerical quadrature in fact yields excellent prediction of $\beta(Pr)$ at $Pr \gtrsim 0.125$, consistently with all approximations noted previously. The high-*Pr* asymptote (dash-dotted line), yields an accurate prediction only at $Pr \gtrsim 10$, whereas the low-*Pr* asymptote tends to overpredict the magnitude of $\beta$ (which is negative for $Pr < 0.5$).

The distributions of the inner-scaled temperature variances are considered in figure 12(*a*), showing substantial growth with the Prandtl number. Specifically, a prominent peak is observed within the buffer layer at high *Pr*, which becomes weaker and moves farther from the wall at lower *Pr*. This behaviour is obviously consistent with the spectra shown in figure 5, as the variances are simply the integrals of the spectral maps over all wavelengths. The change of the peak temperature variance can be estimated by preliminarily noting that asymptotic consistency implies

$$\langle \theta^2 \rangle^+ \overset{y^+ \to 0}{\sim} (b_\theta \, Pr \, y^+)^2, \tag{3.17}$$

**965** A7-17

where $b_\theta$ could in general depend on the Prandtl number (Kawamura *et al.* 1998), but fitting the DNS data suggests $b_\theta \approx 0.245$, regardless of $Pr$. Assuming that quadratic growth of the variance continues up to the peak position, we can estimate that

$$\langle\theta^2\rangle^+_{PK} \approx (b_\theta \, Pr \, \delta^+_t)^2, \tag{3.18}$$

where $\delta^+_t$ is defined in (3.9). Hence the high-Prandtl-number asymptotic behaviour follows

$$\langle\theta^2\rangle^+_{PK} \approx \frac{b^2_\theta A^{4/3}_\theta}{k^{2/3}_\theta} \, Pr^{4/3}, \tag{3.19}$$

whereas (3.10) would yield a constant asymptotic behaviour at low $Pr$, namely

$$\langle\theta^2\rangle^+_{PK} \approx \frac{b^2_\theta}{k^2_\theta}. \tag{3.20}$$

Equation (3.19) is in fact found to be quite successful in predicting the growth of the peak variance, whereas large deviations from the predicted trends are observed at $Pr \lesssim 1$. This is due partly to previously noted difficulties in predicting the behaviour of $\delta_t$ at low $Pr$, but mainly to loss of validity of first-order Taylor series expansion as the peak position moves farther from the wall, and in fact the peak occurs at $y^+ \approx 400$ at $Pr = 0.00625$ (see figure 10). Furthermore, the dominance of thermal conduction at $Pr \ll 1$ implies that thermal fluctuations become vanishingly small in the limit.

The production term of temperature variance, defined as

$$P^+_\theta = \langle u_r \theta \rangle^+ \frac{\mathrm{d}\Theta^+}{\mathrm{d}y^+}, \tag{3.21}$$

is shown in figure 13(*a*). Similar to the temperature variance, it exhibits a prominent peak that decreases in magnitude and moves away from the wall as $Pr$ decreases. It is noteworthy that whereas its magnitude is a strongly increasing function of $Pr$ near the wall, it tends to become very much universal in the outer wall layer (say, $y^+ \gtrsim 100$), as highlighted in figure 13(*b*). The peak production can be estimated on the grounds that the mean thermal balance equation (3.7) implies that for $Re_\tau \to \infty$, $P_{\theta PK} \to 0.25 \, Pr$. However, at any finite Reynolds number, the multiplicative constant is a bit less, and in the present case ($Re_\tau = 1140$) we find

$$P_{\theta PK} = 0.236 \, Pr. \tag{3.22}$$

Figure 13(*c*) shows that this prediction is very well satisfied at $Pr \gtrsim 0.0625$.

### 3.3. *Heat transfer coefficients*

The primary subject of engineering interest in the study of thermal flows is the heat transfer coefficient at the wall, which can be expressed in terms of the Stanton number,

$$St = \frac{\alpha \left\langle \dfrac{\mathrm{d}T}{\mathrm{d}y} \right\rangle_w}{u_b \, (T_m - T_w)} = \frac{1}{u^+_b \theta^+_m}, \tag{3.23}$$

where $T_m$ is the mixed mean temperature (Kays *et al.* 1980),

$$T_m = 2 \int_0^R r \, \langle u_z \rangle \, \langle T \rangle \, \mathrm{d}r \left/ \left( u_b R^2 \right), \right. \tag{3.24}$$
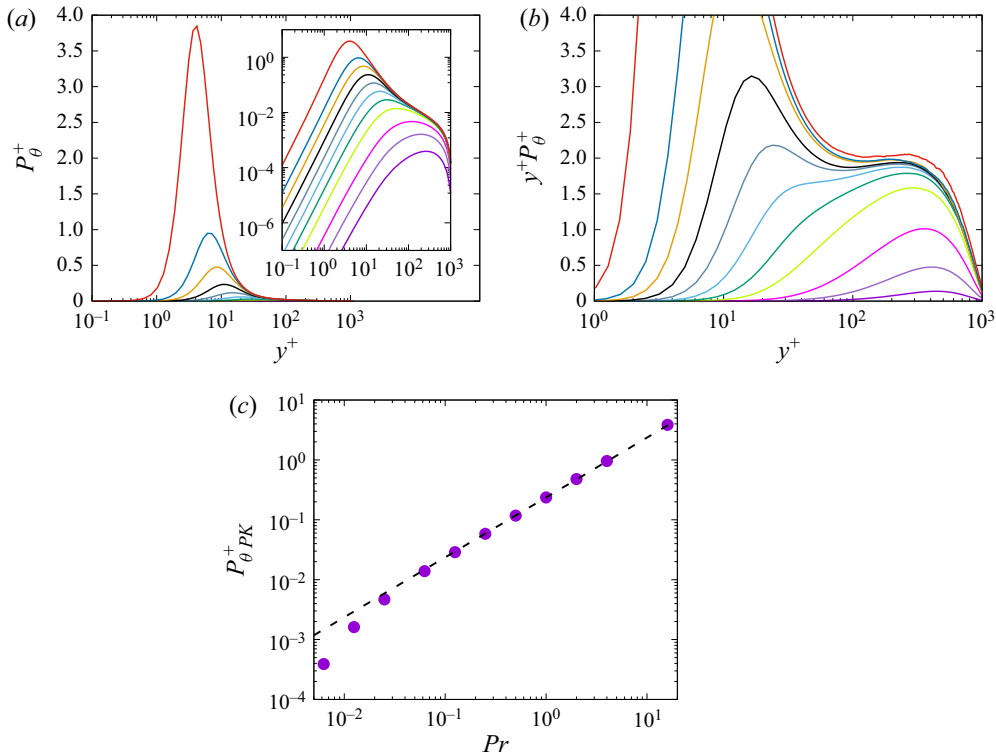
Figure 13. Production of (*a*) temperature variances, also (*b*) pre-multiplied, and (*c*) corresponding peak value as a function of *Pr*. In (*b*), the dashed line denotes the high-*Pr* asymptote (3.22). Refer to table 1 for colour codes.

and $\theta_m^+ = (T_m - T_w)/T_\tau$, or more frequently in terms of the Nusselt number,

$$Nu = Re_b \, Pr \, St. \tag{3.25}$$

A predictive formula for the heat transfer coefficient in wall-bounded turbulent flows was derived by Kader & Yaglom (1972), based on assumed strictly logarithmic variation of the mixed mean temperature with $Re_\tau$,

$$\frac{1}{St} = \frac{2.12 \log \left( Re_b \sqrt{\lambda/4} \right) + 12.5 \, Pr^{2/3} + 2.12 \log Pr - 10.1}{\sqrt{\lambda/8}}, \tag{3.26}$$

where the friction factor $\lambda = 8/u_b^{+2}$ is obtained from the Prandtl friction law, and the log-law offset function was determined based on asymptotic consistency considerations, and by fitting a large number of experimental data, to obtain $\beta(Pr) = 12.5 \, Pr^{2/3} + (1/k_\theta) \log Pr - 5.3$, with $1/k_\theta = 2.12$. The above formula was reported to be accurate for $Pr \gtrsim 0.7$.

A modification to Kader's formula was proposed by Pirozzoli *et al.* (2022), to account more realistically for the dependence of $\theta_m^+$ on $Re_\tau$, resulting in

$$\frac{1}{St} = \frac{k}{k_\theta} \frac{8}{\lambda} + \left( \beta_{CL} - \beta_2 - \frac{k}{k_\theta} B \right) \sqrt{\frac{8}{\lambda}} + \beta_3, \tag{3.27}$$
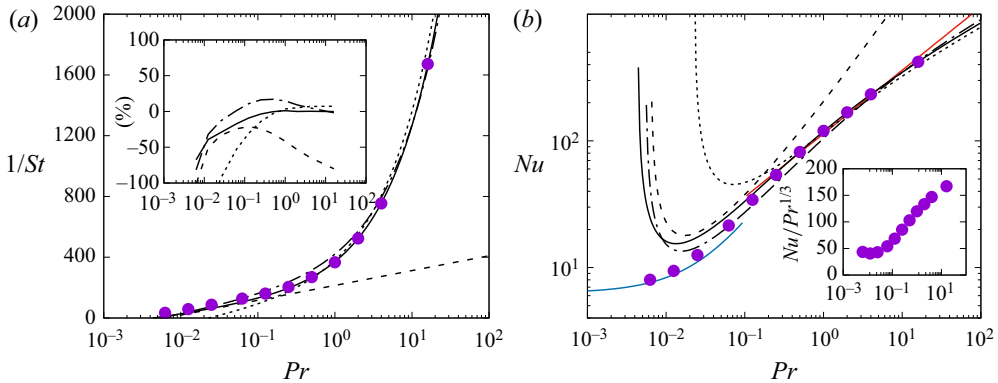
Figure 14. Variation of (*a*) inverse Stanton number and (*b*) Nusselt number, with Prandtl number. The solid lines denote the prediction of (3.27) with $\beta$ defined as in (3.12), whereas the dash-dotted and dashed lines refer to the same equation with $\beta$ obtained from the asymptotic high-*Pr* expression (3.16) and the asymptotic low-*Pr* expression (3.14), respectively. The dotted line refers to Kader's original formula (3.26). The inset in (*a*) shows percent deviations from the DNS data. In (*b*), the red line denotes the correlation (3.28), and the blue line denotes the correlation (3.30). The inset in (*b*) shows the distribution of the Nusselt number obtained from the DNS in compensated form, namely $Nu/Pr^{1/3}$.

where $\beta_{CL}(Pr) = \beta(Pr) + 3.504 - 1.5/k_\theta$, $\beta_2 = 4.92$, $\beta_3 = 39.6$ and $B = 1.23$. Any one of the relations (3.12), (3.14) and (3.16) can then be used to obtain predictions for the heat transfer coefficient variation with the Prandtl number.

The above options are tested in figure 14, which shows the predicted inverse Stanton number (figure 14*a*) and Nusselt number (figure 14*b*). With little surprise, we find that (3.27) with 'correct' definition of $\beta(Pr)$ as in (3.12), yields very good prediction of the heat transfer coefficient, with relative error less than 1 %, for $Pr \gtrsim 0.5$. Larger errors are found at lower *Pr*, at which the assumption of logarithmic distribution of the mean temperature becomes less and less accurate. Larger errors are also obtained with the asymptotic formulations of $\beta(Pr)$ for high and low Prandtl numbers, as well as with Kader's original formula. The figure also shows that the classical power-law correlation (red line) of Kays *et al.* (1980), namely

$$Nu = 0.022\,Re_b^{0.8}\,Pr^{0.5}, \tag{3.28}$$

predicts reasonably the trend of the heat transfer coefficient in the range of Prandtl numbers around unity, whereas it strongly deviates at lower *Pr*, and at higher *Pr*, where (3.27) with (3.16) implies that the correct asymptotic trend is

$$Nu \sim Pr^{1/3}, \tag{3.29}$$

hence shallower than the power-law formulas in common use. The tendency to this asymptotic limit is found to be rather slow, as shown in the inset of figure 14(*b*), and probably data at higher Prandtl numbers would be desirable to corroborate this prediction. Semi-empirical correlations for the Nusselt number in the range $Pr \ll 1$ are available based on studies of heat transfer in liquid metals and molten salts (Lyon & Poppendiek 1954; Yu-ting *et al.* 2009; Pacio, Marocco & Wetzel 2015). One of the most frequently used correlations is the one due to Sleicher & Rouse (1975), namely

$$Nu = 6.3 + 0.0167\,Re^{0.85}\,Pr^{0.93}, \tag{3.30}$$

**965** A7-20

which is shown as a blue line in figure 14(*b*). The agreement with the DNS data is not entirely satisfactory, although it seems to improve as *Pr* decreases. Discrepancies are likely due to the large uncertainty that is associated with experiments in liquid metals (Kader & Yaglom 1972), and/or to potential differences between conditions of imposed heat flux and imposed temperature difference. All in all, it seems that the range of low Prandtl numbers in forced convection has been studied only cursorily in DNS, while certainly deserving much more attention.

## 4. Concluding comments

We have analysed the behaviour of passive scalars in turbulent pipe flow in a wide range of Prandtl numbers, so as to be representative of both the low- and high-Prandtl-number asymptotic limits. Whereas studies at $Pr = O(1)$ are relevant as being representative of air and most gases, Prandtl numbers much lower than unity are frequent in nuclear engineering, being relevant for liquid metals and molten salts used in the cooling systems of nuclear reactors and in solar energy systems, and Prandtl numbers higher than unity are representative of water, oils and diffusing substances in mass transfer processes. At the same time, the friction Reynolds number considered here ($Re_\tau \approx 1140$) is high enough that a near-logarithmic layer is observed in the mean axial velocity, hence we believe that the results are representative of realistic fully developed forced turbulence. We are not aware of any previous DNS study of pipe flow in such wide range of *Pr*, and/or (relatively) high Reynolds number. DNS at $Pr \gg 1$ here have been particularly challenging from a computational standpoint, because of the presence of sub-Kolmogorov scales, which should be accurately accounted for, by resolving the relevant Batchelor scale.

Qualitative results regarding the organization of passive scalars at non-unit Prandtl number generally confirm the findings of previous studies carried out in plane channels (Alcántara-Ávila *et al.* 2018; Abe & Antonia 2019; Alcántara-Ávila & Hoyas 2021), namely that structural similarity with the axial velocity field resulting from similarity of the corresponding transport equations is severely impaired. In fact, strong diffusion at low *Pr* has the effect of filtering out the small scales in the passive scalar field, with special reference to the buffer layer. Hence the corresponding spectral maps (see figure 5) fail entirely to show the near-wall energetic site, whereas the outer energetic site survives even at very low *Pr*. This observation carries potential implications as the temperature field of liquid metals could be used in experiments to track the dynamics of the outer-layer structures, whose importance in the high-*Re* behaviour of boundary layers has been the subject of intensive research (see e.g. Marusic *et al.* 2010). On the other hand, passive scalars at high *Pr* exhibit strong small-scale activity confined to the buffer layer, and near-wall organization into streaks, but with size slightly different than in the unit Prandtl number case. Interestingly, no clear large-scale organization is found in that case, suggesting that the high-*Pr* fluids can be used to study the near-wall layer in isolation from the outer layer.

Regarding the one-point statistics, we find that the mean scalar profiles in the overlap layer can be approximated conveniently with logarithmic distributions, with the exception of cases with very low Prandtl number. Specifically, we provide a criterion for the presence of a logarithmic layer to be $Pe_\tau = Pr\,Re_\tau \gtrsim 11$, which is supported from the DNS data. An accurate model for predicting the mean scalar profiles at any given *Pr* is then formulated by noting very near universality of the distribution of the eddy diffusivity across a wide range of Prandtl numbers ($Pr \gtrsim 0.125$), which can be modelled faithfully in terms

**965** A7-21

of a simple functional relationship. This observation suggests that modelling turbulent diffusion processes directly in terms of the eddy diffusivity can have significant advantage over traditional approaches based on introduction of the turbulent Prandtl number, which has a much more complex spatial distribution.

The model derived for $\alpha_t$ bears the further advantage of yielding predictions for a number of thermal boundary layer statistics. First, we manage to determine estimates for the thickness of the conductive sublayer, which we find to scale as $Pr^{-1/3}$ at high $Pr$, and as $Pr^{-1}$ at low $Pr$, in good agreement with the DNS data. Second, we obtain predictions for the log-law additive constant, which we predict to scale as $Pr^{2/3}$ in the high-$Pr$ limit, in agreement with Kader & Yaglom (1972), and as $\log Pr$ at moderately low Prandtl number. These scalings are well verified in the DNS data. We also obtain predictions for the peak temperature variance and its associated peak production, which we find to scale as $Pr^{4/3}$ and $Pr^1$, respectively, in very good agreement with the DNS data. In general, predictions for the high-$Pr$ behaviour of the flow statistics are quite robust, whereas lack of universality at low $Pr$ makes modelling and theoretical prediction a much more difficult task.

Finally, we have focused on heat transfer. Starting from a modified version of Kader's classical formula (Pirozzoli *et al.* 2022), we have incorporated Prandtl number effects through the log-law offset function. The resulting predictions are in very good agreement with the DNS data, with errors of less than 1 % at $Pr \gtrsim 0.5$, and, consistent with Kader's inferences, we find convincing evidence that the Nusselt number should scale as $Nu \sim Pr^{1/3}$ at high $Pr$, although the approach to the asymptotic trend is quite slow. Predictions, however, become rapidly poorer at low Prandtl number. Conventional power-law approximations (e.g. Kays *et al.* 1980) are in satisfactory agreement with the DNS data at Prandtl number not too far from unity, but they tend to overestimate $Nu$ significantly at $Pr \gtrsim 10$. Other empirical formulas, meant to fit experimental data for liquid metals (e.g. Sleicher & Rouse 1975), provide reasonable approximation of the DNS data only at extremely low $Pr$, whereas they fall short at moderately low $Pr$.

Overall, the present analysis supports and corroborates the theoretical framework set by Kader & Yaglom (1972), at least for fluids with relatively high Prandtl number, removing most doubts raised in previous DNS studies, which were carried out mainly at limited Reynolds number. Furthermore, we are able to set precise operational ranges for the validity of classical heat transfer correlations, which are rather narrow indeed. Most difficulties and uncertainties are associated with the low Prandtl number regime, which features substantial deviations from universality and/or from logarithmic behaviour, thus making the analysis more difficult than for the high-$Pr$ regime. Interesting hints for possible treatment of this regime were given by Abe & Antonia (2019) for plane channel flow, which we plan to expand in future publications. For that purpose, additional DNS at low $Pr$ and higher Reynolds number should be carried out, to verify quantitatively the theoretical prediction that at low $Pr$ the heat transfer coefficient should be a function of solely $Pe = Pr\,Re_b$, and derive suitable scaling laws for the eddy diffusivity. Equally important would be extending the range of Prandtl numbers to higher values. Indeed, as one can infer from figure 14, the tendency of the Nusselt number towards the expected $Pr^{1/3}$ asymptotic behaviour is quite slow. Given that Prandtl numbers in the order of hundreds are important in applications, e.g. engine oils and contaminants, DNS in that range would be highly desirable. Although this would imply prohibitive resolutions using the same grid spacing for the momentum and scalar transport equations, the problem could be circumvented by employing a dual mesh, as done by Ostilla-Mónico *et al.* (2015) for natural convection.

**965** A7-22

**Declaration of interest.** The author reports no conflict of interest.

**Data availability statement.** The data that support the findings of this study are openly available at the web page http://newton.dma.uniroma1.it/database.

**Author ORCIDs.**

Sergio Pirozzoli https://orcid.org/0000-0002-7160-3023.

REFERENCES

ABE, H. & ANTONIA, R.A. 2009 Near-wall similarity between velocity and scalar fluctuations in a turbulent channel flow. *Phys. Fluids* **21**, 025109.

ABE, H. & ANTONIA, R.A. 2017 Relationship between the heat transfer law and the scalar dissipation function in a turbulent channel flow. *J. Fluid Mech.* **830**, 300–325.

ABE, H. & ANTONIA, R.A. 2019 Mean temperature calculations in a turbulent channel flow for air and mercury. *Intl J. Heat Mass Transfër* **132**, 1152–1165.

ABE, H., KAWAMURA, H. & MATSUO, Y. 2004 Surface heat-flux fluctuations in a turbulent channel flow up to $Re_\tau = 1020$ with $Pr = 0.025$ and 0.71. *Intl J. Heat Fluid Flow* **25**, 404–419.

AHN, J., LEE, J.H., LEE, J., KANG, J.-H. & SUNG, H.J. 2015 Direct numerical simulation of a 30R long turbulent pipe flow at $Re_\tau = 3000$. *Phys. Fluids* **27**, 065110.

AKSELVOLL, K. & MOIN, P. 1996 An efficient method for temporal integration of the Navier–Stokes equations in confined axisymmetric geometries. *J. Comput. Phys.* **125**, 454–463.

ALCÁNTARA-ÁVILA, F. & HOYAS, S. 2021 Direct numerical simulation of thermal channel flow for medium-high Prandtl numbers up to $Re_\tau = 2000$. *Intl J. Heat Mass Transfer* **176**, 121412.

ALCÁNTARA-ÁVILA, F., HOYAS, S. & PÉREZ-QUILES, M.J. 2018 DNS of thermal channel flow up to $Re_\tau = 2000$ for medium to low Prandtl numbers. *Intl J. Heat Mass Transfer* **127**, 349–361.

ALCÁNTARA-ÁVILA, F., HOYAS, S. & PÉREZ-QUILES, M.J. 2021 Direct numerical simulation of thermal channel flow for $Re_\tau = 5000$ and $Pr = 0.71$. *J. Fluid Mech.* **916**, A29.

ANTONIA, R.A., ABE, H. & KAWAMURA, H. 2009 Analogy between velocity and scalar fields in a turbulent channel flow. *J. Fluid Mech.* **628**, 241–268.

ANTORANZ, A., GONZALO, A., FLORES, O. & GARCIA-VILLALBA, M. 2015 Numerical simulation of heat transfer in a pipe with non-homogeneous thermal boundary conditions. *Intl J. Heat Fluid Flow* **55**, 45–51.

BATCHELOR, G.K. 1959 Small-scale variation of convected quantities like temperature in turbulent fluid. Part 1. General discussion and the case of small conductivity. *J. Fluid Mech.* **5**, 113–133.

CEBECI, T. & BRADSHAW, P. 1984 *Physical and Computational Aspects of Convective Heat Transfer*. Springer.

DITTUS, F.W. & BOELTER, L.M.K. 1933 Heat transfer in automobile radiators of the tubular type. *Intl Commun. Heat Mass Transfer* **12**, 3–22.

GOWEN, R.A. & SMITH, J.W. 1967 The effect of the Prandtl number on temperature profiles for heat transfer in turbulent pipe flow. *Chem. Engng Sci.* **22**, 1701–1711.

HARLOW, F.H. & WELCH, J.E. 1965 Numerical calculation of time-dependent viscous incompressible flow of fluid with free surface. *Phys. Fluids* **8**, 2182–2189.

HOYAS, S. & JIMÉNEZ, J. 2006 Scaling of velocity fluctuations in turbulent channels up to $Re_\tau = 2003$. *Phys. Fluids* **18**, 011702.

HUTCHINS, N. & MARUSIC, I. 2007 Evidence of very long meandering features in the logarithmic region of turbulent boundary layers. *J. Fluid Mech.* **579**, 1–28.

JIMÉNEZ, J 2018 Coherent structures in wall-bounded turbulence. *J. Fluid Mech.* **842**, P1.

JIMÉNEZ, J. & PINELLI, A. 1999 The autonomous cycle of near-wall turbulence. *J. Fluid Mech.* **389**, 335–359.

JOHNSON, D.A. & KING, L.S. 1985 A mathematically simple turbulence closure model for attached and separated turbulent boundary layers. *AIAA J.* **23**, 1684–1692.

KADER, B.A. 1981 Temperature and concentration profiles in fully turbulent boundary layers. *Intl J. Heat Mass Transfer* **24**, 1541–1544.

KADER, B.A. & YAGLOM, A.M. 1972 Heat and mass transfer laws for fully turbulent wall flows. *Intl J. Heat Mass Transfer* **15**, 2329–2351.

KAWAMURA, H., ABE, H. & MATSUO, Y. 1999 DNS of turbulent heat transfer in channel flow with respect to Reynolds and Prandtl number effects. *Intl J. Heat Fluid Flow* **20**, 196–207.

KAWAMURA, H., OHSAKA, K., ABE, H. & YAMAMOTO, K. 1998 DNS of turbulent heat transfer in channel flow with low to medium-high Prandtl number. *Intl J. Heat Fluid Flow* **19**, 482–491.

KAYS, W.M., CRAWFORD, M.E. & WEIGAND, B. 1980 *Convective Heat and Mass Transfer*. McGraw-Hill.

KIM, J. & MOIN, P. 1985 Application of a fractional-step method to incompressible Navier–Stokes equations. *J. Comput. Phys.* **59**, 308–323.

KIM, J. & MOIN, P. 1989 Transport of passive scalars in a turbulent channel flow. In *Turbulent Shear Flows* (ed. J.-C. André, J. Cousteix, F. Durst, B.E. Launder, F.W. Schmidt & J.H. Whitelaw), vol. 6, pp. 85–96. Springer.

KIM, J., MOIN, P. & MOSER, R.D. 1987 Turbulence statistics in fully developed channel flow at low Reynolds number. *J. Fluid Mech.* **177**, 133–166.

KLINE, S.J., REYNOLDS, W.C., SCHRAUB, W.C. & RUNSTADLER, F.A. 1967 The structure of turbulent boundary layers. *J. Fluid Mech.* **30**, 741–773.

LEE, M. & MOSER, R.D. 2015 Direct simulation of turbulent channel flow layer up to $Re_\tau = 5200$. *J. Fluid Mech.* **774**, 395–415.

LEVICH, V.G. 1962 *Physicochemical Hydrodynamics*. Prentice Hall.

LYON, R.M. & POPPENDIEK, H. 1954 Liquid-Metal Heat Transfer. In *Liquid-Metals Handbook* (ed. R.N. Lyon *et al.*), p. 184. US Government Printing Office.

MARUSIC, I., MCKEON, B.J., MONKEWITZ, P.A., NAGIB, H.M., SMITS, A.J. & SREENIVASAN, K.R. 2010 Wall-bounded turbulent flows at high Reynolds numbers: recent advances and key issues. *Phys. Fluids* **22**, 065103.

MONIN, A.S. & YAGLOM, A.M. 1971 *Statistical Fluid Mechanics: Mechanics of Turbulence*, vol. 1. MIT.

NA, Y., PAPAVASSILIOU, D.V. & HANRATTY, T.J. 1999 Use of direct numerical simulation to study the effect of Prandtl number on temperature fields. *Intl J. Heat Fluid Flow* **20**, 187–195.

NAGANO, Y. & TAGAWA, M. 1988 Statistical characteristics of wall turbulence with a passive scalar. *J. Fluid Mech.* **196**, 157–185.

ORLANDI, P., BERNARDINI, M. & PIROZZOLI, S. 2015 Poiseuille and Couette flows in the transitional and fully turbulent regime. *J. Fluid Mech.* **770**, 424–441.

ORLANDI, P. & FATICA, M. 1997 Direct simulations of turbulent flow in a pipe rotating about its axis. *J. Fluid Mech.* **343**, 43–72.

OSTILLA-MÓNICO, R., YANG, Y., VAN DER POEL, E.P., LOHSE, D. & VERZICCO, R. 2015 A multiple-resolution strategy for direct numerical simulation of scalar turbulence. *J. Comput. Phys.* **301**, 308–321.

PACIO, J., MAROCCO, L. & WETZEL, T. 2015 Review of data and correlations for turbulent forced convective heat transfer of liquid metals in pipes. *Heat Mass Transfer* **51**, 153–164.

PILLER, M. 2005 Direct numerical simulation of turbulent forced convection in a pipe. *Intl J. Numer. Meth. Fluids* **49** (6), 583–602.

PIROZZOLI, S. 2014 Revisiting the mixing-length hypothesis in the outer part of turbulent wall layers: mean flow and wall friction. *J. Fluid Mech.* **745**, 378–397.

PIROZZOLI, S., BERNARDINI, M. & ORLANDI, P. 2016 Passive scalars in turbulent channel flow at high Reynolds number. *J. Fluid Mech.* **788**, 614–639.

PIROZZOLI, S. & ORLANDI, P. 2021 Natural grid stretching for DNS of wall-bounded flows. *J. Comput. Phys.* **439**, 110408.

PIROZZOLI, S., ROMERO, J., FATICA, M., VERZICCO, R. & ORLANDI, P. 2021 One-point statistics for turbulent pipe flow up to $Re_\tau \approx 6000$. *J. Fluid Mech.* **926**, A28.

PIROZZOLI, S., ROMERO, J., FATICA, M., VERZICCO, R. & ORLANDI, P. 2022 DNS of passive scalars in turbulent pipe flow. *J. Fluid Mech.* **940**, A45.

REDJEM-SAAD, L., OULD-ROUISS, M. & LAURIAT, G. 2007 Direct numerical simulation of turbulent heat transfer in pipe flows: effect of Prandtl number. *Intl J. Heat Fluid Flow* **28** (5), 847–861.

RUETSCH, G. & FATICA, M. 2014 *CUDA Fortran for Scientists and Engineers*. Elsevier.

RUSSO, S. & LUCHINI, P. 2017 A fast algorithm for the estimation of statistical error in DNS (or experimental) time averages. *J. Comput. Phys.* **347**, 328–340.

SAHA, S., CHIN, C., BLACKBURN, H.M. & OOI, A.S.H. 2011 The influence of pipe length on thermal statistics computed from DNS of turbulent heat transfer. *Intl J. Heat Fluid Flow* **32** (6), 1083–1097.

SCHWERTFIRM, F. & MANHART, M. 2007 DNS of passive scalar transport in turbulent channel flow at high Schmidt numbers. *Intl J. Heat Fluid Flow* **28**, 1204–1214.

SLEICHER, C.A. & ROUSE, M.W. 1975 A convenient correlation for heat transfer to constant and variable property fluids in turbulent pipe flow. *Intl J. Heat Mass Transfer* **18**, 677–683.

STRAUB, S., FOROOGHI, P., MAROCCO, L., WETZEL, T. & FROHNAPFEL, B. 2019 Azimuthally inhomogeneous thermal boundary conditions in turbulent forced convection pipe flow for low to medium Prandtl numbers. *Intl J. Heat Fluid Flow* **77**, 352–358.

SUBRAMANIAN, C.S. & ANTONIA, R.A. 1981 Effect of Reynolds number on a slightly heated turbulent boundary layer. *Intl J. Heat Mass Transfer* **24**, 1833–1846.

TENNEKES, H. & LUMLEY, J.L. 1972 *A First Course in Turbulence*. MIT.

TOWNSEND, A.A. 1976 *The Structure of Turbulent Shear Flow*, 2nd edn. Cambridge University Press.

VERZICCO, R. & ORLANDI, P. 1996 A finite-difference scheme for three-dimensional incompressible flows in cylindrical coordinates. *J. Comput. Phys.* **123**, 402–414.

WU, X. & MOIN, P. 2008 A direct numerical simulation study on the mean velocity characteristics in turbulent pipe flow. *J. Fluid Mech.* **608**, 81–112.

YU-TING, W., BIN, L., CHONG-FANG, M. & HANG, G. 2009 Convective heat transfer in the laminar–turbulent transition region with molten salt in a circular tube. *Exp. Therm. Fluid Sci.* **33**, 1128–1132.